Article

Molecular Cell

Condensin- and Replication-Mediated Bacterial Chromosome Folding and Origin Condensation Revealed by Hi-C and Super-resolution Imaging

Graphical Abstract

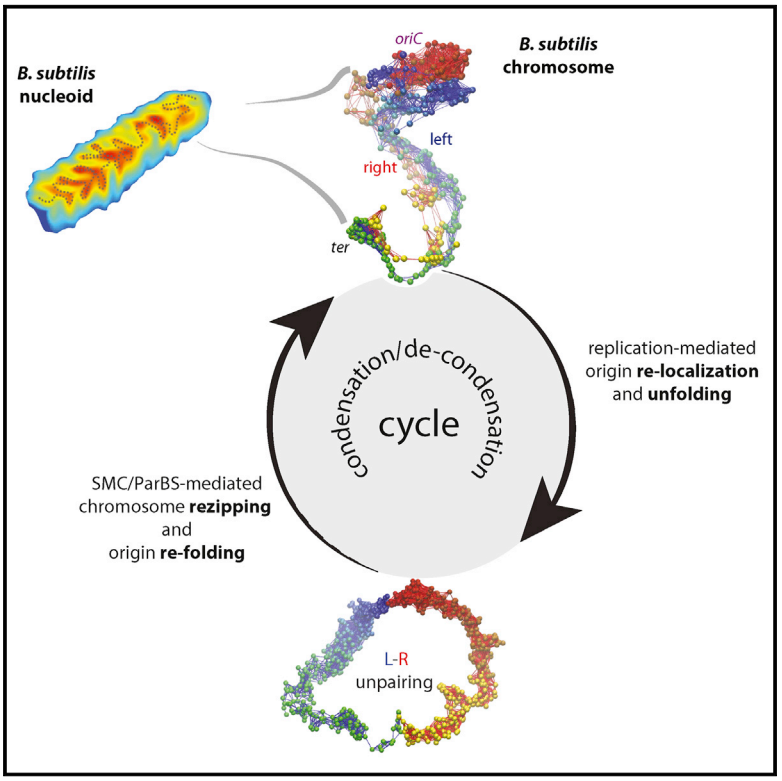

Highlights

- *B. subtilis* chromosome arms are fully zipped by condensin-like complexes
- Architecture of the origin domain may play a role in the regulation of replication
- The origin domain dynamically unfolds and refolds in concert with DNA replication
- Origin folding requires condensin and the bacterial mitotic-like partition system

Authors

Martial Marbouty, Antoine Le Gall, Diego I. Cattoni, ..., Heath Murray, Romain Koszul, Marcelo Nollmann

Correspondence

romain.koszul@pasteur.fr (R.K.), marcelo.nollmann@cbs.cnrs.fr (M.N.)

In Brief

Marbouty et al. combine super-resolution microscopies and chromosome-capture technologies to unveil the higher-order organization of the *Bacillus subtilis* chromosome. They describe the dynamic rearrangements of the origin domain architecture during the cell cycle and dissect the molecular mechanisms and processes involved.

Marbouty et al., 2015, Molecular Cell *59*, 588–602
August 20, 2015
http://dx.doi.org/10.1016/j.molcel.2015.07.020

Marbouty M, LeGall A, Cattoni DI, Cournac A, Koh A, Fiche JB, Mozziconacci J, Murray H, Koszul R, Nollmann M. Condensin- and replication-mediated bacterial chromosome folding and origin condensation revealed by Hi-C and super-resolution imaging. *Molecular Cell* 2015, 59(4), 588-602.

CellPress

Molecular Cell
Article

Condensin- and Replication-Mediated Bacterial Chromosome Folding and Origin Condensation Revealed by Hi-C and Super-resolution Imaging

Martial Marbouty,[1,2,6] Antoine Le Gall,[3,6] Diego I. Cattoni,[3] Axel Cournac,[1,2] Alan Koh,[4] Jean-Bernard Fiche,[3] Julien Mozziconacci,[5] Heath Murray,[4] Romain Koszul,[1,2,*] and Marcelo Nollmann[3,*]

[1]Institut Pasteur, Department of Genomes and Genetics, Group Spatial Regulation of Genomes, 75015 Paris, France
[2]CNRS, UMR 3525, 75015 Paris, France
[3]Centre de Biochimie Structurale, CNRS UMR5048, INSERM U1054, Université de Montpellier, 29 Rue de Navacelles, 34090 Montpellier, France
[4]Centre for Bacterial Cell Biology, Institute for Cell and Molecular Biosciences, Newcastle University, NE2 4AX Newcastle Upon Tyne, UK
[5]Laboratoire de Physique Théorique de la Matière Condensée, CNRS UMR 7600, Université Pierre et Marie Curie, Sorbonne Universités, 75005 Paris, France
[6]Co-first author
*Correspondence: romain.koszul@pasteur.fr (R.K.), marcelo.nollmann@cbs.cnrs.fr (M.N.)
http://dx.doi.org/10.1016/j.molcel.2015.07.020

SUMMARY

Chromosomes of a broad range of species, from bacteria to mammals, are structured by large topological domains whose precise functional roles and regulatory mechanisms remain elusive. Here, we combine super-resolution microscopies and chromosome-capture technologies to unravel the higher-order organization of the *Bacillus subtilis* chromosome and its dynamic rearrangements during the cell cycle. We decipher the fine 3D architecture of the origin domain, revealing folding motifs regulated by condensin-like complexes. This organization, along with global folding throughout the genome, is present before replication, disrupted by active DNA replication, and re-established thereafter. Single-cell analysis revealed a strict correspondence between sub-cellular localization of origin domains and their condensation state. Our results suggest that the precise 3D folding pattern of the origin domain plays a role in the regulation of replication initiation, chromosome organization, and DNA segregation.

INTRODUCTION

Ensuring the proper propagation of chromosomes over generations is a complex process essential to the survival and evolution of all living organisms. Regulatory mechanisms have evolved to coordinate replication, segregation, and cell division, concomitantly with other DNA-related metabolic processes such as transcription. Within the last 10 years, chromosome conformation-capture (3C) technologies (Dekker et al., 2002) have started to unveil new levels of chromosomal hierarchical organization at the megabase and sub-megabase scales. Topological domains (TDs) have originally been defined in higher eukaryotes as genomic regions within which the chromatin fiber displays a high frequency of preferential contacts (Dixon et al., 2012; Sexton et al., 2012). TD-like domains have been described as well in bacteria, where they were defined as chromosomal interaction domains (CIDs) (Le et al., 2013).

Functional roles of topological domains are poorly understood. In particular, it is ignored whether their architecture may affect or be affected by other cellular functions such as DNA replication and segregation. This interplay is especially acute in bacteria, which lack the well-characterized segregation apparatus of eukaryotes. Several mechanisms have been suggested to promote sister segregation, such as passive disentangling thanks to tethering to the cell envelope, active segregation by partition complexes, or mechanical "stress" relief models (Kleckner et al., 2014).

Structural maintenance of chromosomes (SMCs) are ubiquitous complexes implicated at different hierarchical levels of chromosomal organization as well as in replication and transcription. In eukaryotes, SMC complexes play different roles depending on their protein composition: cohesins are responsible for holding sister chromatids together after replication, whereas condensins ensure faithful segregation through compaction and organization of sister chromatids at the late stages of mitosis (Nasmyth and Haering, 2009). The large majority bacterial clades possess canonical SMC-kleisin-like complexes composed of two SMC subunits, a kleisin (ScpA) and a third factor (ScpB). Most bacteria with SMC-ScpAB complexes also encode a partitioning system with three essential components: a centromere site (*parS*), a centromere-binding protein (ParB), and a Walker-type ATPase (ParA). ParB bound to *parS* recruits SMC-ScpAB complexes to the origin of replication region (Gruber and Errington, 2009; Sullivan et al., 2009), and their combined action contributes to the resolution of newly replicated origins (Gruber et al., 2014; Wang et al., 2014b). In *Bacillus subtilis* (*B. subtilis*), the chromosome adopts a strict oriC-ter-oriC longitudinal orientation for most of the cell cycle (Berkmen and Grossman, 2006; Wang et al., 2014a). Interestingly, replication origins are

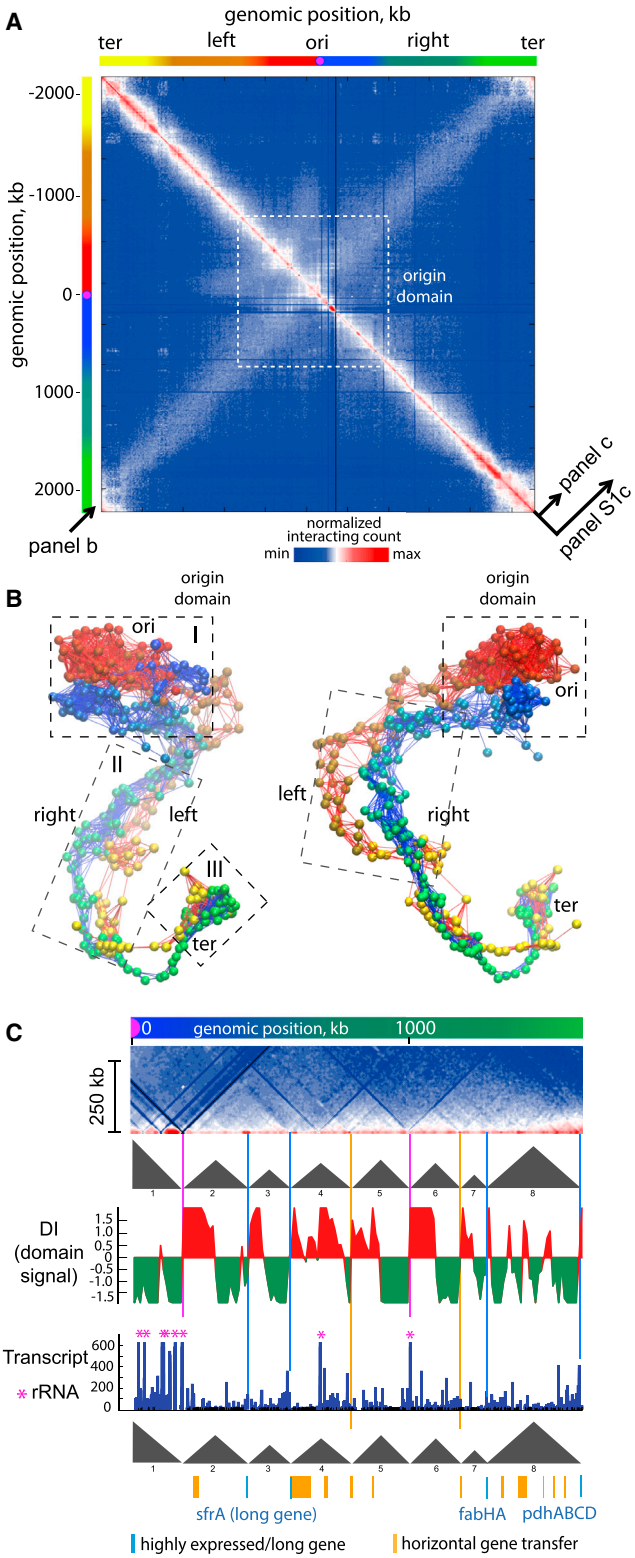

Figure 1. Whole-Chromosome Organization in *B. subtilis*

(A) Normalized genomic contact map obtained from an asynchronous population (rich medium). X and y axes represent genomic coordinates centered at *oriC* (pink circle). Left and right arms are represented by red-yellow and blue-green gradients. Black arrows outline features of interest described in (B), (C), and Figure S1C. White dashed box represents the origin domain as defined in (B). The colorscale reflects the frequency of contacts between two regions of the genome (a.u.), from blue (rare contacts) to red (frequent contacts), and is conserved across all panels of all figures to facilitate reading. Strain: HM1320.

(B) 3D representation of the contact map from (A). The chromosome is represented as a chain of beads (1 bead = 4 kb; see Supplemental Experimental Procedures). Bead color-coding reflects linear genomic position along the chromosome (same as in A). Dotted squares highlight broad global domains (see text). See also Movie S1.

(C) Top panel: magnification of contacts within a 250 kb window of the right chromosomal arm. Middle panel: DI analysis of the corresponding genomic region. Downstream (red) and upstream (green) biases are indicated. CIDs are represented as gray triangles. Lower panel: transcription signal (Nicolas et al., 2012). Genomic annotations of highly expressed genes (light-blue rectangles), horizontal gene-transfer elements (yellow rectangles), and rRNA genes (purple asterisks) are indicated. Blue, yellow, and purple vertical lines represent barriers between domains coinciding with these elements. See also Figures S1A and S1C.

located on the nucleoid poles in newborn cells, and, following replication initiation, the duplicated origins are transiently relocalized to the center of the new nucleoids before being actively segregated to opposite positions at the nucleoid edges (Wang et al., 2014a).

Here, we used a unique combination of super-resolution microscopies and chromosome conformation capture (Hi-C) to shed light into the higher-order structure of the *B. subtilis* chromosome and unveil the factors responsible for its regulated folding. This approach revealed the fine 3D architecture of a large domain encompassing the origin of replication, the cycles of origin domain condensation/de-condensation coupled to replication and sub-cellular localization, and the specific roles of the ParABS system, the SMC-ScpAB complex, and active replication in defining global chromosome architecture and origin domain folding.

RESULTS

Higher-Order Chromosome Organization in *B. subtilis*

To investigate chromosome organization in *B. subtilis*, we applied chromosome conformation capture analysis to exponentially growing wild-type (WT) cultures in rapid growth conditions. The resulting contact map (Figure 1A) shows a strong and broad diagonal reflecting frequent local contacts resulting from interactions among adjacent loci. Several additional notable features emerge upon further analysis.

Three Broad Global Domains

Overall chromosome topology is revealed by converting the contact map into a 3D topological representation (Figure 1B and Movie S1) (Lesne et al., 2014). The nucleoid folds into a helicoidal shape, analogous to that also seen in *E. coli* (Fisher et al., 2013; Hadizadeh Yazdi et al., 2012) and *C. crescentus* (Umbarger et al., 2011). Within this folding pattern, three distinct sub-regions (hereafter referred to as "domains") can be discerned, each containing portions of the left and right chromosome arms. First, a large globular region of ~1.4 Mbp encompasses the origin of replication (origin domain, Figure 1B, box I). This domain is directly visible in the contact map as a region displaying a large

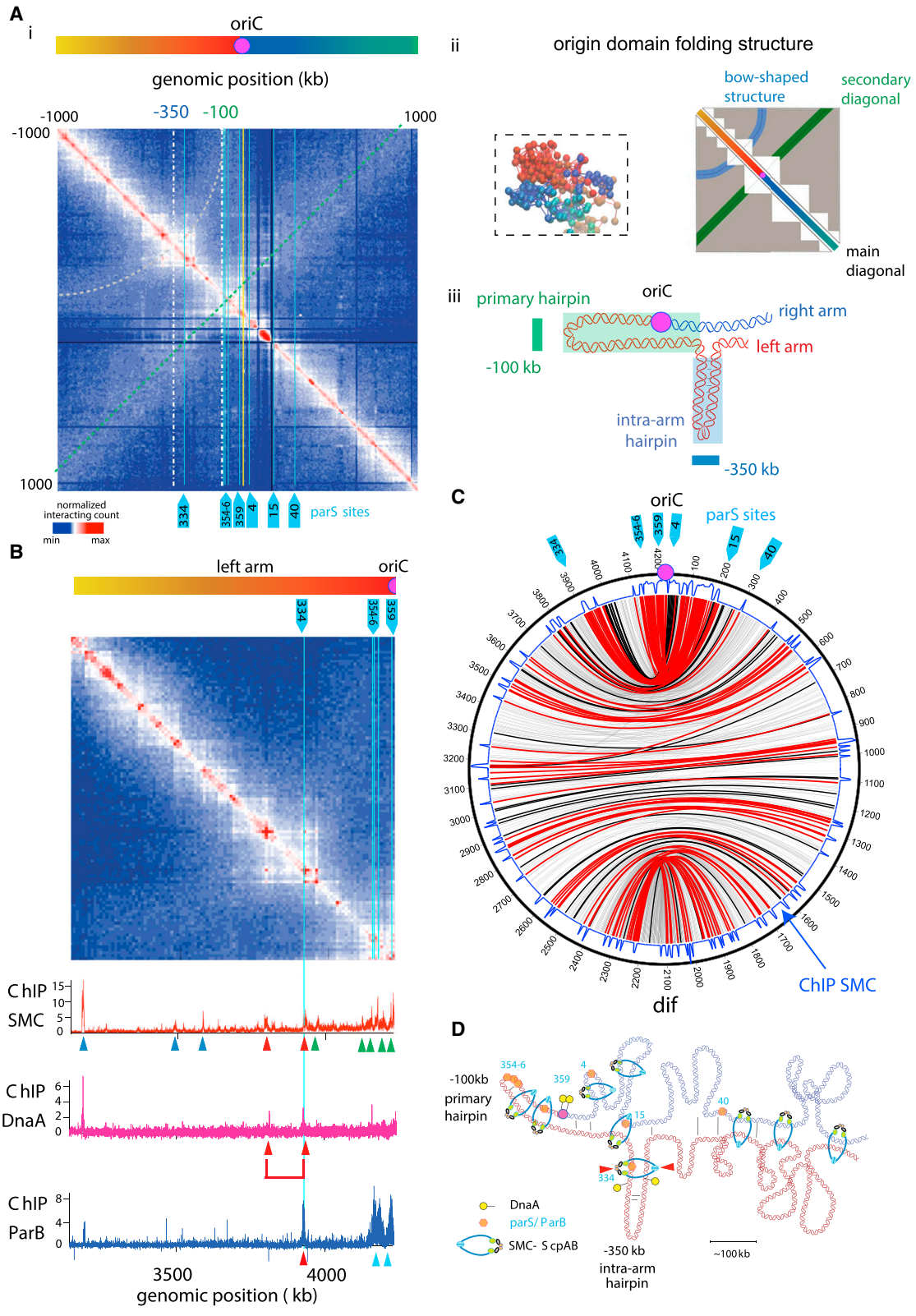

(legend on next page)

number of inter- and intra-arm contacts around oriC (Figure 1A, dashed box). Second, a broad middle region of the genome exhibits very close juxtaposition of the two arms (Figure 1B, box II). This feature is directly visible in the primary contact map as a distinctive secondary diagonal (perpendicular to the main diagonal, Figure 1A). Finally, a smaller domain of ~500 kb encompasses the terminus of replication (ter) region (Figure 1B, box III).

Local, Short-Range Domains

An expanded view of the main diagonal reveals squares of various sizes (Figure 1C). This feature implies the presence of local domains that reflect contacts over a range of genomic distances. The smaller domains, defined by contacts at short correlation lengths, were analyzed with respect to size, number, and borders using the directionality index (DI) approach (Dixon et al., 2012) (Figures 1C and S1A). DI analysis reveals the presence of regions in which contacts are absent, i.e., "barriers." Regions between barriers are inferred to define contact subdomains. Over the entire chromosome, we observed 20 statistically significant barriers, implying the existence of at least ~20 interaction domains ranging in size from 50 to 300 kb (mean at 175 ± 50 kb, Figure S1A). This pattern was not significantly affected by the genotypes of the strains used (PY79 or BS168A, Figure S1B). 60% (12/20) of the barriers coincided with highly expressed genes. This correlation, previously described in *C. crescentus* (Le et al., 2013), suggests that transcription may hinder interactions of loci that flank the transcribed region (Figure 1C). However, not all highly expressed genes generated detectable barriers to interactions. Conversely, a number of regions in the genome generate barriers that do not overlap with transcription hotspots. Interestingly, these regions correspond principally to DNA elements acquired through horizontal transfer that present a low GC% compared to the rest of the genome and are specifically bound by the transcriptional activator Rok (Figure S1A). Such sequences represented ~30% of the barriers. Short-range interaction patterns were severely disrupted by the treatment of cells with rifampicin, a general transcription inhibitor (Figure S1B). Irrespective of local influences of transcription, this effect points to an important positive role for transcription in maintenance of global chromosome organization, possibly via its effects on DNA supercoiling (Higgins, 2014).

Organizational and/or Temporal Complexity in Middle-Range Genomic Distances

The primary contact map is unusually complex at middle-range genomic distances, with a complicated array of partially overlapping squares (or, in half-contact maps, triangles) (Figure S1C, triangles). This pattern could result from a tendency for complex, simultaneous contacts comprising "nested" domains, with smaller domains interacting with one another and/or embedded within larger domains. Alternatively, it could reflect heterogeneity within the population, with different types of contacts in different cells or at different stages of the cell cycle (e.g., below).

DI analysis provides one description of this complex pattern of domains. This approach directly detects barriers, not domains (above); nonetheless, different combinations of domains with different genomic sizes can lead to the formation of barriers (Figure S1C, triangles). For the sake of simplicity, and in analogy to domains described in *C. crescentus*, all of the different-sized domains defined by DI barrier analysis will be referred to as "chromosome interaction domains" (CIDs).

Internal Architecture of the Origin Domain

Next, we analyzed the organization of the large origin domain revealed by the contact map and the 3D reconstruction (above). Magnification of the contact map reveals a well-defined substructure comprised of a pair of nested hairpin structures (Figure 2A). The main hairpin results directly from inter-arm contacts linking the left and right replichores genome-wide (above; Figure 2A). Importantly, these contacts do not originate at oriC, but rather at a genomic region ~100 kb to the left of oriC. We will refer to this folding motif as the primary hairpin. A second detected signal suggests the presence of an intra-arm hairpin. This type of motif is manifested in an array of contacts that extend away from the main diagonal as a bow-shaped signal that skews toward the left (away from the origin). The intra-arm hairpin originates at ~−350 kb on the contact map (Figure 2A). The effect of these hairpins is to bring distant genomic loci on the left replichore into close proximity of oriC. Notably, *parS*^{334} is contained within this hairpin and appears to form a sequence-specific loop with a genomic locus located ~125 kb away along the left arm (Figures 2A and 2B). The same detailed folding of the origin domain is seen in a variety of growth media (Figure S1C). These

Figure 2. Structural Organization of the Origin Domain

(A) (i) Magnification of the normalized genomic contact matrix from Figure 1A encompassing an ~2,000 kb region around oriC. Yellow solid line indicates the position of the origin. Positions of *parS* sites are indicated as cyan boxes and lines. Secondary diagonal and bow-shaped structures passing through −100 and −350 kb, respectively, are indicated by blue and green dotted lines, while the coordinates at which they cross the main diagonal are shown by white dotted lines. (ii) 3D representation of the origin domain (left) and schematic representation of the main elements in the contact map (right). (iii) Schematic representation of the putative folding of part of the origin domain. Strain: HM1320.

(B) Contact map from 1,200 kb to *oriC*. *ParS* site positions are indicated as cyan solid lines throughout. ChIP-chip enrichment profiles for SMC-ScpAB, DnaA, and ParB are displayed under the contact map (red, pink, blue, respectively). Red arrowheads and lines highlight the enrichment of SMC-ScpAB, DnaA, and ParB on the specific contact made by *parS*^{334}. Green arrowheads indicate peaks of SMC-ScpAB in the vicinity of oriC. Blue arrowheads indicate peaks of SMC-ScpAB far from *oriC*. Strain: HM1320.

(C) Circos plot representation of genome-wide contacts and the ChIP profile of SMC-ScpAB (Supplemental Experimental Procedures). Outer ring: chromosome coordinates (kb). Inner blue profile: SMC-ScpAB enrichment. Only inter-arm contacts (secondary diagonal) were used. Light-gray lines: subset of inter-arm contacts randomly selected. Red lines: contacts between two genomic sites enriched in SMC-ScpAB. Black lines: contacts between one region enriched in SMC-ScpAB and a non-enriched region. Strain: HM1320.

(D) Schematic representation of the putative average structure of the origin domain. Right and left replichores are represented in blue and red, respectively, with pink and yellow circles representing oriC and dnaA boxes. ParB/*parS* complexes are shown as orange hexagons with their chromosomal positions displayed in degrees. SMC-ScpAB complexes are represented as blue/green tweezers.

signals suggest an average origin domain organization with two hairpins that regroup several *parS* sites to the vicinity of oriC (diagram, Figure 2A).

The SMC-ScpAB Complex and the ParBS System Are Implicated in the Formation and Maintenance of Origin Domain Architecture

Positioning of parS *Sites, ParB, SMC-ScpAB, and DnaA Enrichment Sites within the Origin Domain*

To understand the possible factors involved in defining origin domain architecture, we aligned Hi-C contact maps and ChIP protein enrichment profiles for ParB, SMC-ScpAB, and DnaA within the origin region (Figure 2B) (Breier and Grossman, 2007; Gruber and Errington, 2009; Ishikawa et al., 2007). A cluster of three *parS* sites ($parS^{354,355,356}$) is located close to the tip of the primary hairpin, and a strong SMC-ScpAB enrichment is observed at this cluster and at flanking positions (Gruber and Errington, 2009) (Figure 2B, green arrowheads).

In addition, SMC-ScpAB is enriched at other specific positions. A notable example is provided by a region of sequence-specific contacts between the two sides of the intra-arm hairpin (Figure 2B, red arrowheads), visualized in the contact map as a dot away from the main diagonal. This specific contact is flanked on one side by $parS^{334}$ and on the other side by a genomic locus located ~125 kb away along the left arm. Interestingly, these two genomic loci are bound by the replicator initiator protein DnaA (Ishikawa et al., 2007) (Figure 2B). These two distant DnaA boxes are negative regulators of replication initiation (Okumura et al., 2012). Thus, this specific contact and the primary and intra-arm hairpins could serve to bring distant DnaA boxes close to OriC to regulate origin firing (Figure 2B).

Strikingly, and more generally, SMC-ScpAB complexes are enriched at genomic positions displaying symmetrical inter-arm contacts that extend from the $parS^{354\text{-}356}$ locus to the terminus of replication (Figure 2C, red lines). This specific enrichment is consistent with a global, functional "pairing" between arms mediated by SMC-ScpAB.

Taken together, these findings suggest a model in which the origin domain is specifically folded into a nested structure with at least ParB, SMC-ScpAB, and DnaA participating in the formation of long-range contacts along entire chromosome arms, local intra-arm contacts within the origin domain, and sequence-specific long-range contacts. A schematic representation synthesizes the folding motifs and contacts described (Figure 2D).

Absence of parS*, ParB, or SMC-ScpAB Results in Unfolding of the Origin Domain*

To determine whether ParABS/SMC-ScpAB are indeed involved in maintaining the organization of the origin domain, we tested the effect of mutants. Strikingly, the contacts resulting from inter- and intra-arm hairpin structures were considerably compromised in the absence of ParB, in a strain without *parS* sites (*parS*-Δ10), or when SMC-ScpAB was depleted, as reflected by the disappearance of perpendicular diagonals at −100 and −350 kb, respectively (Figure 3A). We noticed that specific contacts within the intra-arm hairpin enriched in DnaA were not perturbed, suggesting that other factors may be implicated in the formation of this folding element. In contrast to wild-type (Figure 1B), replichore pairing is disrupted in mutant strains because no inter-arm contacts are observed in ParBS/SMC-ScpAB mutants. Loss of pairing is clearly illustrated by 3D topological representations (Figure 3B and Movie S2). These results are consistent with inter-arm contacts specifically requiring the recruitment of the condensin complex by ParB to the origin region. Thus, the recruitment of SMC-ScpAB to the primary and intra-arm hairpins could drive the overall folding of the chromosome down to the terminus of replication (Figure 2C).

To directly test at the single-cell level whether ParB-recruited SMC-ScpAB complexes are required to bridge inter-arm contacts, we monitored the distance between two loci within the origin domain in vivo. Fluorescent repressor operator array (FROS) tags were located close to $parS^{359}$ and $parS^{334}$, thus marking the opposite sides of the inter-arm contacts detected by Hi-C (Figure 3C). The distance between FROS tags increased by 75% ± 4% in the ΔParB mutant with respect to WT (from 100 ± 95 nm in WT to 175 ± 120 nm in ΔParB, mean ± SD; Figure 3C). Because deletion of ParB decreases proper recruitment of SMC-ScpAB to the origin region (Sullivan et al., 2009), these results are consistent with our proposed role of SMC-ScpAB in mediating inter-arm chromosomal contacts.

Dynamic Folding and Unfolding of the Origin Domain in Concert with DNA Replication

Next, we investigated whether the features identified above for asynchronous cultures were present at all stages of the cell cycle and/or whether they undergo dynamic changes. We therefore generated contact maps for replication-arrested cells (a G1-arrest-like chromosomal state) and throughout their re-start of replication (i.e., release into S phase) using a temperature-sensitive replication initiation mutant (dnaB-ts; Supplemental Experimental Procedures; Figure S2).

When replication initiation is blocked, the origin domain is largely disorganized; the primary hairpin and, to a lesser extent, the intra-arm hairpin are strongly attenuated (Figure 3D). Furthermore, this disorganization extended throughout the chromosome, all the way to the terminus region (Figure S2). These results are consistent with replication-arrested chromosomes following a left-ori/ter-right organization, in agreement with cytological data (Berkmen and Grossman, 2006; Wang et al., 2014a) (Figure 5G).

Following replication re-start, a number of contacts between the two replichores gradually reappear, reaching nearly the original signal observed in asynchronously growing cells after 60 min (Figure 3D). These results demonstrate that a compact, coherent nucleoid organization occurs before and after replication, whereas replication per se is accompanied by global disruption of that organization. The signals and processes involved in coupling of these two processes remain to be defined. The most straightforward possibility is that initiation of DNA replication triggers unfolding of the origin domain; however, it remains unclear whether propagation of this disorganization is mediated by the replication process itself or in some other way (see Discussion).

Single-Cell Super-resolution Analysis Reveals a New Nucleoid Substructural Feature, the "High-Density Chromosomal Regions"

Chromosome conformation capture typically examines bulk populations of cells. As a complement of Hi-C, we used an

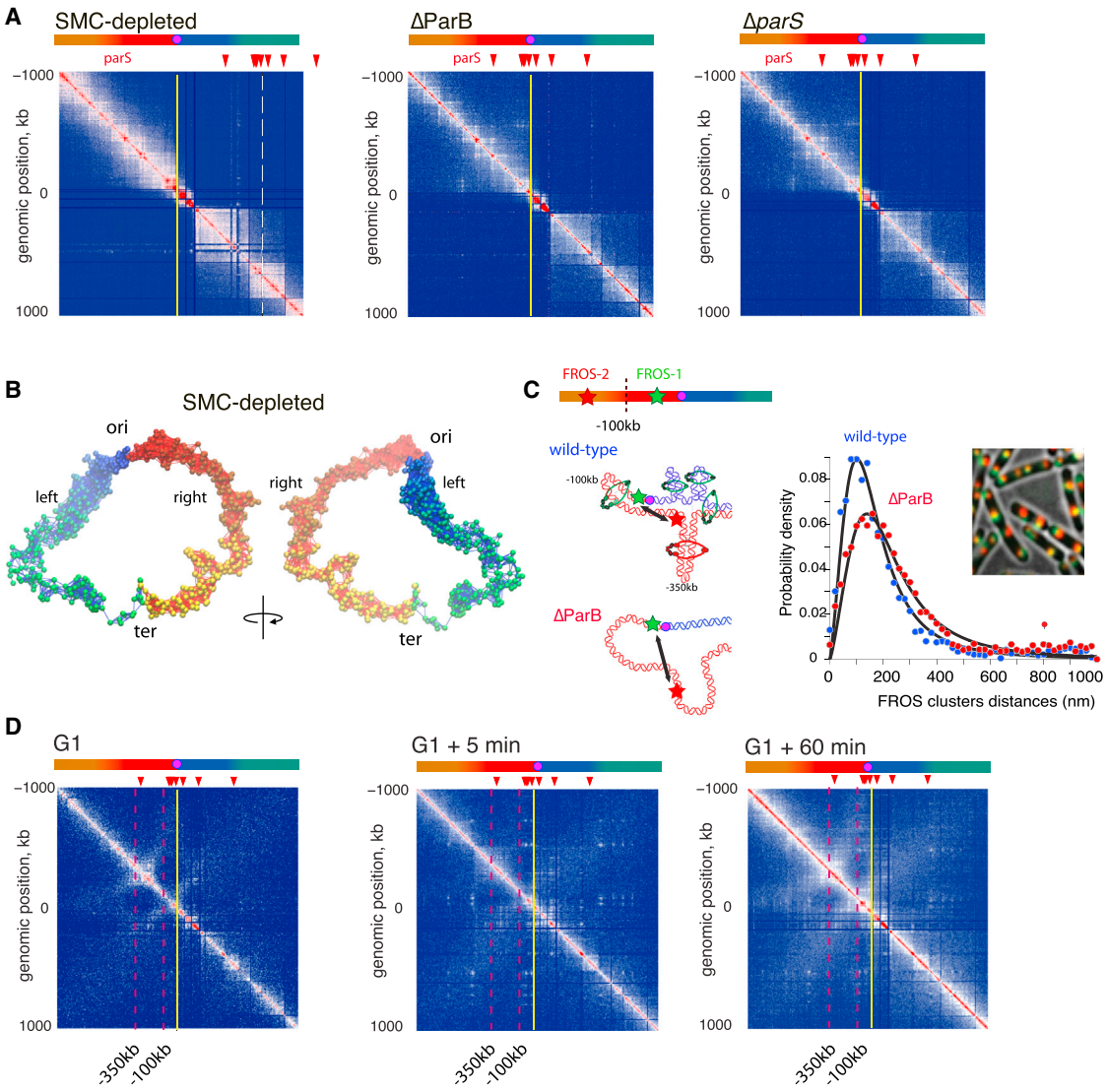

Figure 3. Roles of ParBS, SMC-ScpAB, and Replication in Chromosome Organization

(A) Magnification of the normalized contact maps for SMC-ScpAB-depleted cells, ΔparB, and Δ*parS* mutants (see Figure S2 for full contact maps). Color-codes for chromosome representations (top) and contact frequencies were as in Figure 1A. Red triangles indicate the positions of *parS* sites. Solid yellow lines indicate the position of oriC. Strains: AK487, AK525, and AK215.

(B) Two views of a 3D representation of the contact map of SMC-ScpAB-depleted cells. The chromosome is represented as in Figure 1B. See also Movie S2. Strain: AK487.

(C) Left panels: Effect of ParB in origin domain folding was determined in live cells by measuring the distance between two FROS tags positioned at 359° and 334° (FROS-1 and FROS-2, green and red stars, respectively) in WT and ΔparB cells. Right panel: Distribution of distances between FROS-1 and FROS-2 for WT and ΔParB strains (blue and red dots, respectively). Black solid lines represent a fit to a log-normal distribution. Inset: representative microscopy image of a field of cells (brightfield) superimposed with the fluorescence signals of FROS tags (green and red, respectively). Strains: AK359 and HM923.

(D) Magnification of normalized contact maps for dnaB-ts cells arrested in G1 (left) and released into S phase after 5 min (middle) and 60 min (right) (Figure S2 for full contact maps). Red triangles indicate positions of *parS* sites, and red dotted line indicates the position of the secondary diagonal and the bow-shaped structure at −100 and −350 kb, respectively. Solid yellow lines indicate the *oriC* position in the contact maps. Strain: HM890.

original imaging approach to explore the global 3D organization of the bacterial chromosome in single cells. Building upon recent developments (Fisher et al., 2013; Hadizadeh Yazdi et al., 2012), we combined high-density whole-chromosome labeling with high-throughput, 3D structured illumination microscopy (3D-SIM), which provides a 2-fold increase in spatial resolution as compared to previous wide-field epifluorescence studies. Chromosomes were fluorescently labeled by either chemical staining (DAPI) or by Hbs-GFP, a non-specific DNA-binding protein (Smits and Grossman, 2010). Expression of Hbs-GFP does not perturb chromosome architecture (Figure S2) (Wang et al., 2014a). DAPI is an intercalating dye that could potentially alter

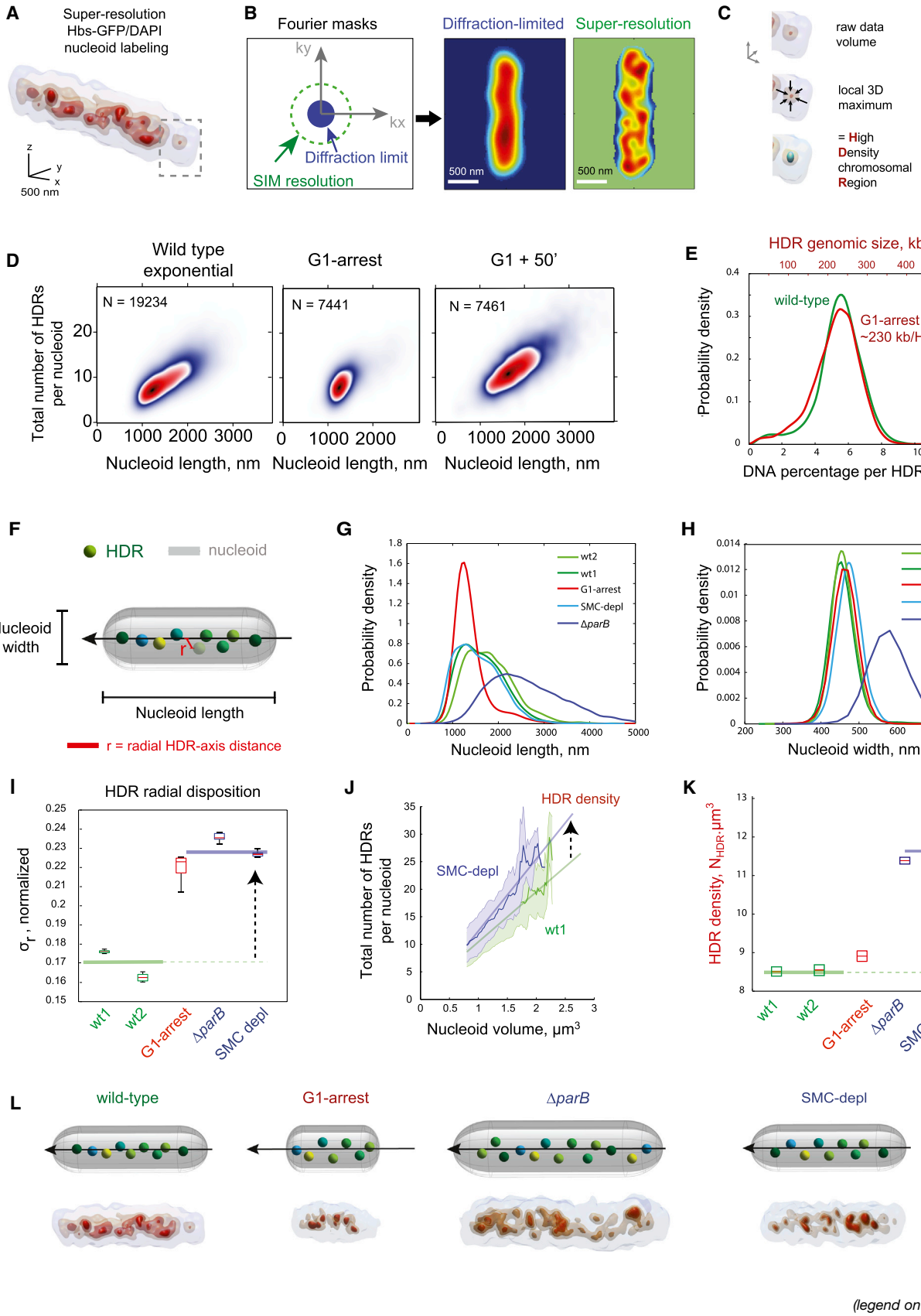

(legend on next page)

nucleoid state. However, we found no significant difference in the patterns given by the two methods (Figure S3A). Together, these approaches provide significantly improved visualization of the 3D organization of nucleoids in living cells (Figure 4A).

3D-SIM images reveal the existence of high-density chromosomal regions (HDRs) organized along the long axis of the cell (Figures 4B, S3B, and S3C). HDRs were defined as 3D positions that display convergent, multi-directional gradients of the intensity signal (Figure 4C and Supplemental Experimental Procedures). HDRs with a size of a single voxel cannot be discerned from camera noise and were discarded. HDRs were not visible in cells in which cytosolic GFP was imaged instead of the nucleoid, implying that they represent true nucleoid signals rather than imaging noise (Figures S3C and S3D). Time-lapse analysis shows that HDRs are relatively stable structures over periods of tens of seconds (Figure S3D). By performing high-throughput super-resolution microscopy on thousands of cells, we obtained statistically significant distributions of the number and cellular localization of HDRs.

For a population of slowly growing cells in exponential phase, the average number of HDRs in newborn nucleoids was 7.9 ± 2.1 (mean ± SD) (Figures 4D, left panel, and S5A). In replication-arrested cells, the average number of HDRs was 8.5 ± 2.2 (mean ± SD) (Figures 4D, middle panel, S5A). After release of the replication block, the number of HDRs increases linearly with nucleoid length, rising to 15 ± 4 HDRs (mean ± SD) detected before cell division, as expected for a doubling of genome content (G1 + 50 min; Figure 4D, right panel). The mean number of HDRs detected for nucleoids in newborn cells also increases from minimal to rich media (Figure S4A), again consistent with a higher chromosome copy number in faster growth rate conditions. These results reveal the existence of a new level of chromosomal sub-organization, made possible by the gain in spatial resolution afforded by 3D-SIM (Figure S3B).

To further quantify these structures, we estimated the average percentage of DNA per HDR from the cumulative fluorescence signal within each HDR and the total nucleoid signal in G1-arrested cells (Figure 4E). Because these cells contain a single chromosome, we estimated semi-quantitatively a reference mean amount of DNA per HDR (~230 kb). Interestingly, the distribution of the percentage of DNA within HDRs in exponentially growing cells for nucleoids of comparable sizes (WT; Figure 4E, green curve) was similar to the distribution in G1, consistent with the mean size of HDRs being conserved between these two states.

The existence of a higher-order nucleoid sub-organization has not previously been reported. It is thus of interest to know whether and/or how HDRs are related to genomically specified organizational features. CIDs comprise DNA domains presenting enriched contacts and are thus expected to be present in condensed regions within the cell. However, HDRs are substantially larger than the average CID as defined above. We therefore imagine that HDRs might arise as a physically based organizational feature that, in addition, may often represent stochastic groupings of CIDs. Preliminary experiments measuring the co-localization of FROS tags within CIDs and HDRs (Figure S4B) are consistent with this hypothesis, which, however, requires extensive further consideration.

We used the new perspective provided by 3D-SIM analyses to further explore the influence of ParABS/SMC-ScpAB and DNA replication on chromosome structure and dynamics. Different parameters were analyzed in WT cells or in cells depleted for SMC-ScpAB, deleted for the parB gene (ΔParB), or arrested in G1 (Figure 4F). Analysis of asynchronous cultures revealed that

Figure 4. High-Density Chromosomal Regions

(A) 3D-SIM volume of a DAPI-stained nucleoid. Light-gray to red colorscale represents low to high DNA densities, respectively. Dotted square highlights the magnified region shown in (C). Scale bar, 500 nm. Strain: PY79. See also Figure S3A.

(B) Left panel: schematic representation of the upper-resolution limits of conventional and 3D-SIM microscopies in Fourier space (solid blue and green dashed circles, respectively). Middle plane of a DAPI-stained nucleoid band-pass filtered using a 3D butterworth low-frequency filter with a spatial cutoff at 200 nm (middle panel), and a band-pass filter with spatial cutoffs at 100 and 400 nm (right panel). Scale bar, 500 nm. Strain: PY79. See also Figure S3B.

(C) Higher DNA-density region from the nucleoid in (A) (dotted square). Black arrows in middle panel represent the directions of the gradient in intensity signal at the position of a local maximum. This local intensity maximum (green sphere in bottom panel) corresponds to an HDR. See also Figure S3C.

(D) 2D kernel density plots of the number of HDRs versus nucleoid length. Left panel: asynchronously growing cells in minimal media. Middle panel: G1-arrested cells. Right panel: cells 50 min after replication block release. N: number of nucleoids analyzed. Strains: PY79 and HM890. See also Figure S5A.

(E) Estimation of HDR DNA content in WT and G1-arrested cells for nucleoids of lengths between 1,200 and 1,400 nm (green and red lines, respectively). The upper x axis describes HDR genomic size estimated from G1-arrested cells (containing a single chromosome) where the genomic content of the full nucleoid is known.

(F) Schematic representation of a single nucleoid (gray cylinder) and automatically detected HDRs represented as colored spheres. The radial distance between the detected HDRs and the nucleoid long axis is indicated by a red arrow.

(G and H) Kernel density distributions of nucleoids length (g) and width (h) for two asynchronously growing WT strains (wt1, wt2), SMC-ScpAB-depleted cells (SMC-depl), ΔParB cells (ΔParB), and synchronized G1-arrested cells. Strains: PY79 (wt1), HM1320, HM671 (wt2), AK488, and AK525.

(I) Boxplot of HDR radial distances normalized by nucleoid width for the same cell lines depicted in (G) and (H). Box represents the first and third inter-quartiles, horizontal bar within the box represents the median, and the error bars represent minimum and maximum of distribution. Radial distances were computed as the mean of a running average (window of 200 nm and step size of 200 nm) of the radial distances of HDRs in nucleoids of lengths comprised between 1,200 and 2,000 nm.

(J) Mean number of HDRs per nucleoid as a function of the nucleoid volume in wild-type cells (wt1, PY79, dark-green solid line) and SMC-ScpAB-depleted cells (SMC-depl., AK488, dark-blue solid line). Nucleoid volumes were computed by summing the number of voxels in each individual nucleoid multiplied by the volume of a voxel (voxel = 2.10^{-4} μm^3). Blue and green shaded areas represent the SD in the number of detected HDRs per nucleoid volume.

(K) HDR density (in number of HDRs per μm^3) for the same cell lines as in (G) and (H). HDR density was estimated as the slope from a linear regression of the total number of detected HDRs per nucleoid as a function of nucleoid volume (see J). See (I) for explanation of boxplot.

(L) Top: schematic representations (similar to the one depicted in F) of nucleoid and HDR spatial distributions for the different cell lines used in (G)–(K). Bottom: corresponding 3D images (similar to the one presented in A) of representative nucleoids for each strain.

nucleoid lengths and widths vary little upon SMC-ScpAB depletion (Figures 4G and 4H). For ΔParB, width and lengths were considerably larger, consistent with the increased activation of replication origins—and thus genomic content—observed in this mutant (Okumura et al., 2012). Replication-arrested cells displayed similar widths but considerably shorter lengths than asynchronous cells (Figures 4G and 4H), consistent with the presence of a single chromosome.

Interestingly, HDRs existed in all conditions, irrespective of the organization suggested by Hi-C. The mean radial distance of HDRs away from the longitudinal nucleoid axis increased for replication-arrested cells and ΔParB/SMC-ScpAB mutants (Figure 4I). Finally, the mean HDR density, defined as the total number of HDRs over the nucleoid volume, remained unchanged in WT cells but increased considerably in absence of ParB or SMC-ScpAB (Figures 4J and 4K). Representative nucleoids and schematic representations of the effects of mutations are summarized in Figure 4L. Overall, these data indicate that the number of HDR per genome equivalent is relatively constant throughout the cell cycle, despite global changes in nucleoid shape over time. The increased numbers and dispersion of HDRs in mutants compared to wild-type possibly reflect a more open conformation of the replichores, consistent with Hi-C data in G1-arrested cells.

The Origin of Replication Is Contained within a Single Prominent HDR that Persists throughout the Cell Cycle

The Hi-C results presented above point to the existence of a large folded origin domain present in G1 that unfolds during S phase and reappears after replication. We next investigated whether the origin domain might correspond to an HDR and, more generally, whether HDRs displayed a conserved sub-cellular localization throughout the cell cycle and between cells. Direct averaging of 3D images of nucleoids of similar sizes led to a blurring of HDR positions, resulting in the loss of structural information (Figure S5A). To overcome this averaging effect, we determined the positions of each HDR in nucleoids along the longitudinal and radial axes. We then computed, for nucleoids of the same size, the (2D) histogram of HDR positions along these two axes (Figure S5A; Supplemental Experimental Procedures). This procedure yielded robust, characteristic patterns of HDR localization with only a few hundred cells (Figure 5A). Despite the presence of ~5–15 HDRs in each cell, only a small number of maxima are observed in the histograms of HDR positions. These maxima represent positions where an HDR occurs with high probability, thus identifying the specific cellular positions where HDRs are more likely to be observed.

HDR positional distributions determined in an asynchronous population were used to evaluate dynamic changes in positional preferences over time in the cell cycle, using increasing nucleoid length as a time metric. This information is displayed, for a given population, as a 2.5D kymograph-like representation (Figures 5B and S5B). In a WT culture growing under slow growth conditions, HDR maxima display a well-defined choreography (Figure 5B, left). The smallest cells exhibit a single prominent local maximum of HDR probability at the center of the nucleoid (darkest red signal in the kymograph and black signal in 2D histograms). As nucleoid size begins to increase, this single HDR maximum splits into two maxima that migrate toward the poles, where they remain for most of the cycle. At a later stage, the two HDR maxima relocalize to the centers of two new discrete nucleoids. Finally, after sister nucleoids split, these maxima migrate to their starting positions at their respective new poles.

The pattern of segregation observed for this maximum HDR density signal corresponds to that expected for the dynamic positioning of the origin region, as defined by previous FROS studies (Berkmen and Grossman, 2007; Wang et al., 2014a). Thus, we refer to this maxima as origin-correlated HDR (ori-HDR). This correlation was directly documented by five further analyses.

First, the segregation pattern of ori-HDRs corresponds to a large degree to that of ParB-GFP (Figures 5C, S5B, and S5C), which is known to bind over the entire origin domain and is normally used as a marker of the oriC position (Sullivan et al., 2009).

Second, we analogously analyzed the positioning of an origin-proximal FROS tag (at 359° on the genome map) and of ParB-GFP in a strain carrying only a single, unique *parS* site at the corresponding position. In both cases, the segregation pattern (blue-red colorscale) closely resembles the trajectory of ori-HDR (Figure 5D, dotted lines). FROS tags in other positions (174°, 240°, and 273°) exhibit very different segregation patterns (Figure 5E).

Third, we directly visualized HDRs and ParB-GFP simultaneously in a strain containing a single *parS* site close to the origin of replication ($parS^{359}$; Figure 5F, left). A striking correlation can be observed between the localization of ori-HDR (represented by the z axis of the distribution) and ParB-GFP signal (colorscale superimposed to the HDR pattern; Figures 5F, right, and S5C).

Fourth, as expected from FROS analysis (Wang et al., 2014a) and Hi-C analysis (above), G1-arrested cells displayed a unique HDR maximum at the center of the nucleoid (Figure 5G, left). After replication re-start, two HDR maxima predominantly relocalized to the edges of the nucleoid (Figure 5G, right), following the re-localization pattern of origins after replication re-start (Wang et al., 2014a).

Fifth, depletion of SMC-ScpAB or deletion of parB, both of which result in disorganization of the origin domain, led to somewhat aberrant segregation patterns of ori-HDRs (Figure S5C).

Taken together, these results strongly suggest that oriC is part of a discrete and dense structure that persists throughout the cell cycle.

Super-resolution Analysis of Origin Domain States

Because *parS* sequences are distributed throughout the origin domain defined by Hi-C, super-resolution visualization of *parS*-bound ParB-GFP provides a proxy to the spatiotemporal dynamics of this domain from a perspective complementary to that of Hi-C (Figure 6A, inset).

3D-SIM and 3D-Photo-Activated Localization Microscopy (PALM) imaging showed that several discrete ParB-GFP sub-clusters group together in a larger ParB cluster in slowly growing, asynchronous WT cells (Figure 6A). The sub-cellular localization and segregation pattern of ParB clusters corresponded to that of oriC (compare Figures 5C and 5D). Thus, each ParB-GFP cluster represents a single origin domain (Figure 6A). ParB-GFP sub-clusters were individually detected and grouped together to

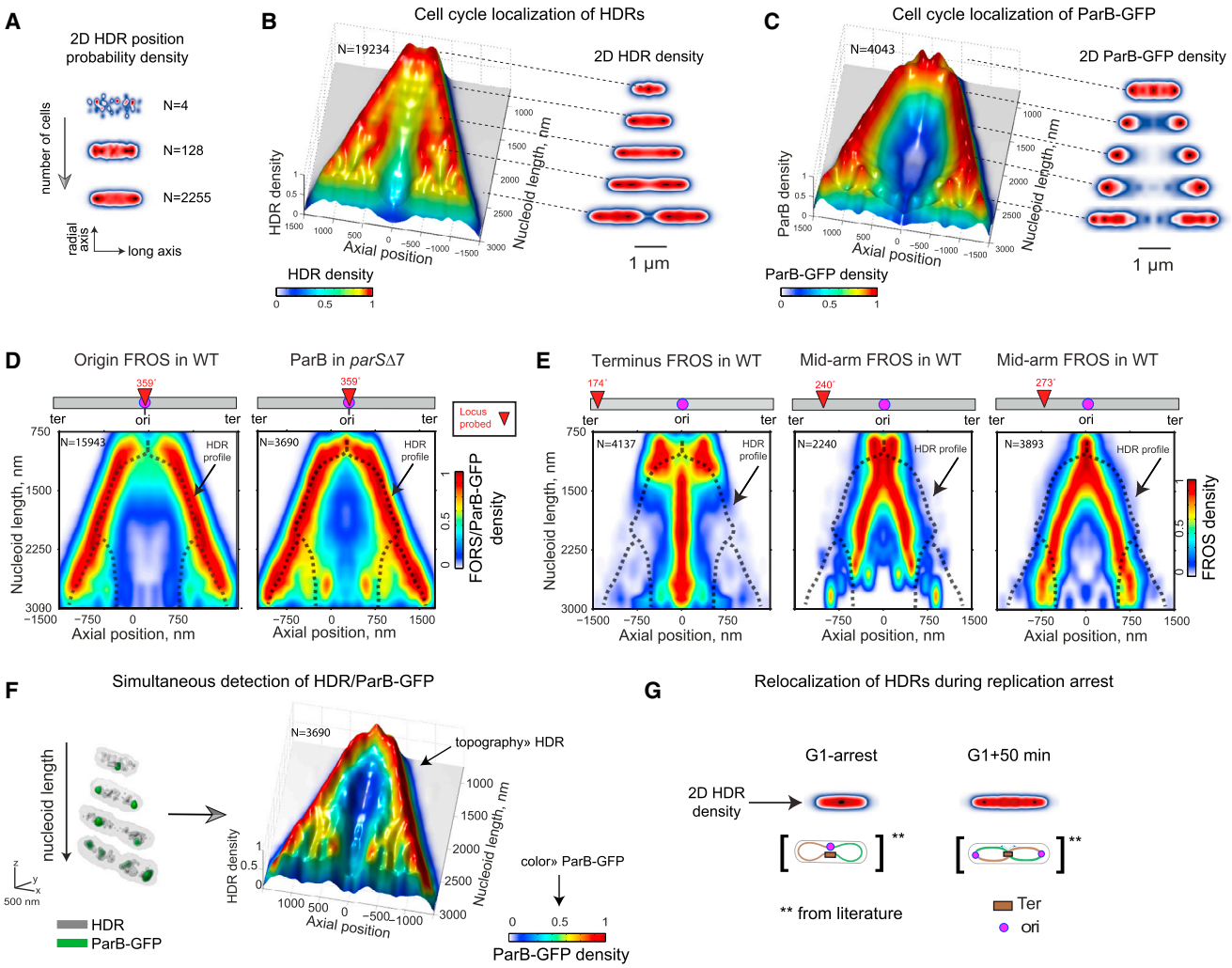

Figure 5. The Spatial Organization of the Nucleoid: Heterogeneity of HDR Distributions

(A) Schematic depicting the procedure for constructing the 2D probability density histograms of HDR positions within nucleoids. HDR coordinates were normalized with respect to each nucleoid and then integrated with HDR coordinates from nucleoids of same length. N: number of nucleoids analyzed for each 2D histogram. See Supplemental Experimental Procedures and Figure S5A.

(B) 2.5D kymograph of HDRs localization in DAPI-labeled nucleoids. Axes represent the axial position of HDRs and the nucleoid sizes. Both color map and z axis (i.e., topography) represent HDR localization density. Right panel: 2D density histograms of HDRs for varying nucleoid lengths extracted from the kymograph. N: number of nucleoids analyzed. Strain: PY79. See also Figures S5B and S5C.

(C) 2.5D kymograph of ParB-GFP localization as a function of their axial position and nucleoid length. The kymographs were generated using the same algorithm described in (B), but including all ParB-GFP clusters independently of their radial distances. Right panel: 2D density histograms of ParB-GFP detected in DAPI-labeled nucleoids for varying nucleoid lengths extracted from the kymograph. N: number of nucleoids analyzed. Strain: HM671.

(D and E) Cell-cycle localization kymographs of FROS tags. (D) Labeling of the oriC region in cells either harboring all *parS* sites (origin FROS in WT) or containing a single *parS* site near the origin (ParB-GFP in *parS*Δ7). (E) Labeling of genomic positions located at the ter (Terminus-FROS in WT), at one-third of left arm (Mid-arm FROS in WT), and at a mid-position along the left arm (Mid-arm FROS in WT). Schematic representations of the chromosome are displayed above each kymograph, with the labeled region indicated with a red triangle, and its genomic position in degrees. Dashed lines superimposed to the kymographs provide a guide to the eye for the segregation pattern observed in the kymograph of HDR maxima in (B) (ori-HDR). N: number of nucleoids analyzed. Strains: HM923, HM673, BWX925, BWX1206, and BWX1053.

(F) Simultaneous detection of HDRs and ParB-GFP. Left: typical two-color, representative 3D-SIM images of DAPI-stained single nucleoids and ParB-GFP-labeled origins for cells at different stages of the cell cycle. Nucleoid periphery is shown in light gray, while higher-density regions at the center of the nucleoid are shown in dark gray. ParB-GFP complexes, localizing to the origins of replication, are represented in green. Right: 2.5D kymograph of HDRs with their density represented by the topography (z axis). The superimposed color map represents ParB-GFP intensity extracted from the same nucleoids. N: number of nucleoids analyzed. Strain: HM673. See also Figure S5C.

(G) Re-localization of ori-HDRs during replication arrest and restart. Top: 2D distributions for cells synchronized (left) in G1 arrest and (right) 50 min after release of the replication block (nucleoid lengths between 1,000–1,250 nm and 1,500–1,750 nm, respectively). Bottom: schematic representations depicting the localizations of oriC and ter as well as the right and left chromosomal arms from literature (Wang et al., 2014a). Strain: HM890. See also Figure S5C.

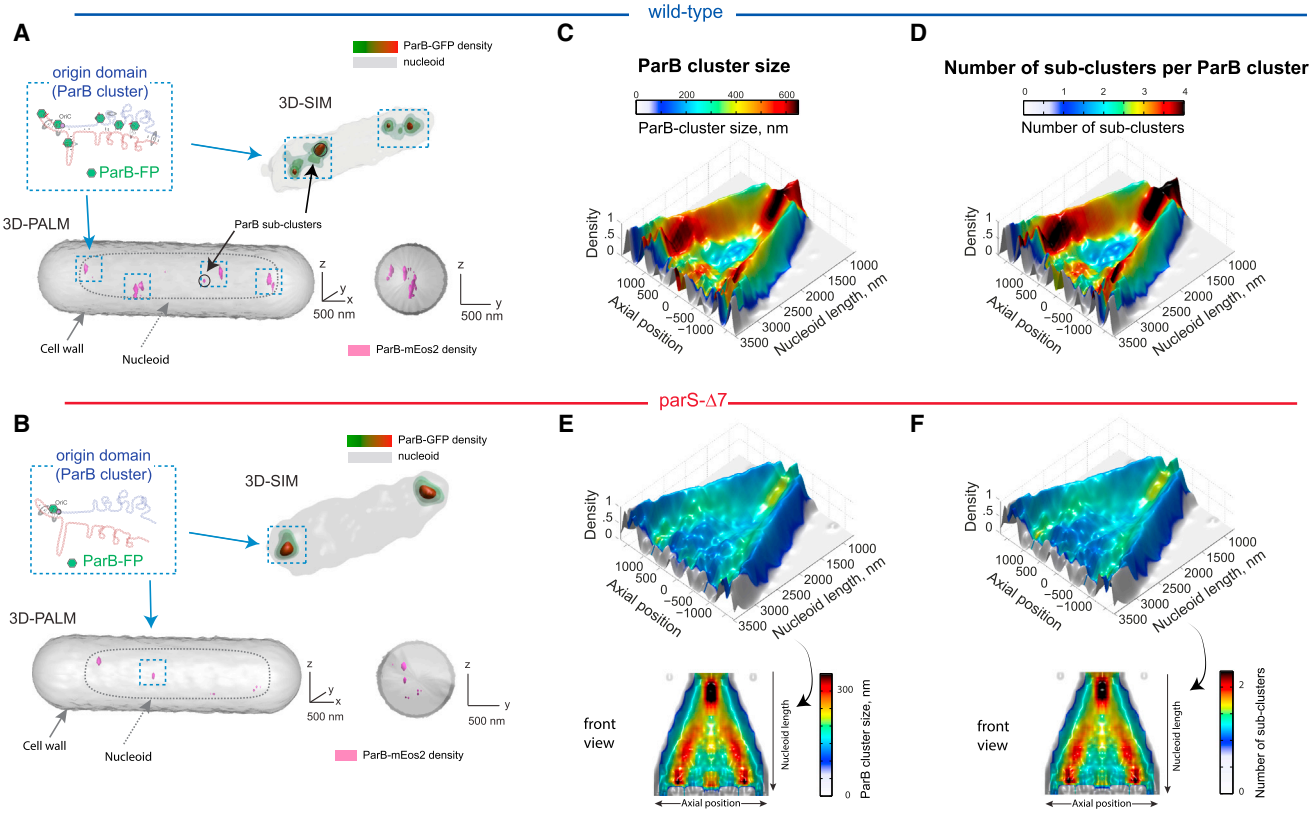

Figure 6. Direct, 3D Visualization of the Organization of the Origin Domain

(A and B) Representative (top) 3D-SIM and (bottom) 3D-PALM images of origin domains labeled with either ParB-GFP (green-red) or ParB-mEos2 (pink). For 3D-SIM images, the nucleoids were visualized by DAPI staining (gray contour), while for 3D-PALM imaging the cell volume was reconstructed from brightfield images (dark-gray contour). (A) The chromosome carries all naturally occurring *parS* sites (wild-type). (B) The chromosome carries a single *parS* site ($parS^{359}$, strain *parS*-Δ7). Dotted square insets depict a schematic representation of the expected enrichment of fluorescently labeled ParB-GFP within the origin domain for wild-type and *parS*-Δ7. Strains: HM671, HM673, HM675, and HM677. See also Figure S6A.

(C–F) 2.5D kymograph of ParB cluster distributions as a function of axial position and nucleoid length. The density of ParB clusters is represented by the topography of the kymograph (i.e., height in the z axis). Color-codes applied to the kymograph and indicated on top of (C) and (D) represent either ParB cluster size (C and E) or the number of ParB-GFP sub-clusters (D and F). Insets in (E) and (F) depict a 2D view of the 2.5D kymographs with a colorscale re-adjusted compared to WT in order to highlight the ParB cluster migration pattern for cells having a single *parS*. Strains: HM671 and HM673. See also Figures S6B and S6C.

determine the number of sub-clusters forming each ParB cluster (Figure S6A). The mean number of ParB-GFP sub-clusters per ParB cluster was 2.8 ± 2 (mean ± SD) (Figure S6B). To validate this approach, we determined the ParB-GFP distribution in a strain carrying only a single *parS* site at the origin ($parS^{359}$, strain *parS*-Δ7). In this case, ParB clusters containing a single (1.2 ± 0.8, mean ± SD), isolated ParB-GFP sub-cluster were visualized (Figures 6B and S6B). These single ParB sub-clusters predominantly localized at nucleoid edges (Figure 5F). The size of ParB-GFP clusters in *parS*-Δ7 corresponded to the resolution limit (Figure S6A). Thus, ParB-GFP clusters in WT cells represent combinations of *parS* sites that group together to form an origin domain.

The validity of this assumption was further confirmed by computing the average number and relative distance between ParB clusters. In both WT and *parS*-Δ7, the number of ParB clusters per nucleoid (1.9 ± 0.6 for WT and 2.0 ± 0.7 for *parS*-Δ7, mean ± SD) and the average maximal distance between ParB clusters (1500 ± 450 nm for WT and 1400 ± 500 nm for *parS*-Δ7, mean ± SD) were consistent with two origin domains located at the edges of the nucleoid in most cells (Figures 5C and S6B) (Berkmen and Grossman, 2007; Wang et al., 2014a).

The size of origin domains in WT cells was then estimated from the distances between the most widely separated ParB-GFP sub-clusters within single ParB clusters. Domain sizes were widely distributed, with an average size of 440 ± 210 nm (mean ± SD) (Figure S6C). ParB cluster sizes were slightly smaller when measured using 3D-PALM due to the higher resolution of this method, cell fixation, and differences in the clustering algorithms used (Figure S6C). Importantly, both estimations were consistent with our previous measurements using FROS tags (Figure 3D). These results suggest that the origin domain is composed of several independent *parS* sites with distinct, resolvable physical positions that likely correspond to the positions of *parS* sites/interactions suggested by Hi-C analysis (Figure 2C).

Next, analysis of the distribution of ParB-GFP cluster sizes and compositions was used to probe for changes in the state of the origin domain during cell-cycle progression. We measured the

changes in the number of ParB sub-clusters per ParB cluster and the sizes of ParB clusters as a function of nucleoid size and sub-nuclear localization (Figures 6C, 6D, and S6C). ParB-GFP cluster density was plotted as a function of nucleoid size and axial positions, resulting in the same type of 2.5D kymograph representation as described above. The colorscale of this density pattern reflects variations either in the number of ParB sub-clusters per ParB cluster or in ParB cluster sizes (Figures 6C, 6D, and S6C). Strikingly, origin domains were highly condensed while positioned at the nucleoid edges, as revealed by the small size and small number of sub-clusters, but displayed a large increase in the number of sub-clusters and size as they approached the centers of new nucleoids (Figures 6C and 6D). A similar trend was observed for *parS*-Δ7 cells, although these cells displayed considerably lower numbers of sub-clusters and sizes (Figures 6E and 6F).

Overall, this pattern of condensation and decondensation of the origin domain corresponds closely to the program of replication-correlated unfolding and refolding of the origin domain defined by Hi-C (Figure 2), as well as that displayed by ori-HDR (Figure 5), suggesting that condensin loading at the origin following replication may participate in the refolding of the origin domain.

DISCUSSION

In this work, we combined Hi-C and super-resolution microscopies to reveal and dissect several important mechanisms and functions of chromosome folding within a model bacterium.

Chromosomal Interaction Domains in *B. subtilis*

Previous Hi-C studies on *C. crescentus* proposed that barriers between CID domains are mainly due to highly transcribed genes blocking the diffusion of free supercoils (Le et al., 2013). This model is consistent with studies in *E. coli* and *Salmonella enterica* showing that transcription activity from strong promoters promotes the formation of topological barriers (Booker et al., 2010; Higgins, 2014). In these species, however, topological barriers were observed at considerably shorter length-scales (~10–15 kb) (Postow et al., 2004), with only very highly transcribed genes (e.g., rrn genes) accounting for ~8% of the detected topological barriers (Booker et al., 2010). Our Hi-C analysis shows that a large proportion of transcription hotspots in the *B. subtilis* chromosome fail to produce detectable barriers between CIDs. Conversely, a considerable number of barriers fail to correlate with regions of high transcriptional activity, but instead overlap with the genomic positions of a nucleoid-associated protein (Rok) (Smits and Grossman, 2010) and of AT-rich sequences acquired through horizontal gene transfer. This specific enrichment of mobile genetic elements at barriers indicates that these genetic loci may be particularly susceptible or permissive to rearrangement events, possibly due to the pause or collapse of replication forks. This enrichment was also observed in higher eukaryotes (Sexton et al., 2012). More investigations are, however, needed to understand whether this signal is truly meaningful or is a side effect of the 3C methodology. Overall, these observations are consistent with several functional activities—besides transcription—playing a role at establishing barriers between CIDs.

HDRs Represent a New Organizational Feature of the Chromosome

Using 3D-SIM combined with whole-chromosome labeling, we discovered a level of chromosome organization (HDRs) that is not visible by diffraction-limited fluorescence microscopy methods (Fisher et al., 2013; Hadizadeh Yazdi et al., 2012; Le et al., 2013). HDRs are substantially larger than the average CID, suggesting that HDRs may often represent stochastic associations of CIDs. FROS tags within CIDs were found to often localize within HDRs, consistent with this hypothesis. Further experiments, however, are needed to establish the specific genomic nature of HDRs. The spatial modulation of chromosome density within HDRs is a key feature that may need to be taken into account to model the physical state of the chromosome. HDRs exist in all cells, but only ori-HDRs display a conserved sub-cellular localization with a well-defined cell-cycle choreography. This observation suggests that the sub-cellular localization of ori-HDR may be specifically regulated, possibly to control replication state and to propagate specific folding patterns from the origin toward the remainder of the chromosome. Further experiments in other species will be required to determine whether HDRs are a universal feature of bacterial chromosomes.

Organization and Potential Function of the Origin Domain

In *B. subtilis*, replication origins localize to the edge of the nucleoid for most of the cell cycle (Figure 5) (Berkmen and Grossman, 2006; Wang et al., 2014a), where they appear highly condensed (Figure 6). Thus, the specific folding pattern captured by Hi-C technologies from an asynchronous population (Figure 2) reflects primarily the structure of origins at this sub-cellular position (Figure 7A). Interestingly, DnaA binds not only to boxes in the oriC-proximal region, but also to six other distant boxes located in intergenic regions (Ishikawa et al., 2007) (Figure 2B). Despite their distance to the origin, intergenic DnaA boxes act to inhibit replication initiation (Okumura et al., 2012; Smits et al., 2011). Our results suggest that the origin domain folding brings distant DnaA boxes in the vicinity of oriC (Figures 2D and 7A), suggesting that origin domain architecture may play a role in the regulation/inhibition of replication initiation.

Dynamics of Origin Domain Folding during the Cell Cycle

The widths and shapes of the primary and intra-arm hairpins suggest that the origin domain has a dynamic and/or heterogeneous architecture (Figure 2A). Our single-cell super-resolution measurements revealed size variations that occur concomitantly with sub-cellular repositioning during the cell cycle (Figures 5 and 6). Recently, Wang et al. suggested that origins are replicated at the nucleoid edges before being repositioned to the middle of new nucleoids, where they embark on bi-directional segregation (Wang et al., 2014a). Origin re-localization seems to be correlated with a re-organization of the chromosome from a longitudinal to a transverse orientation (Wang et al., 2014a). Our microscopy data show that origin domains remain condensed at the nucleoid edges, with origin de-compaction

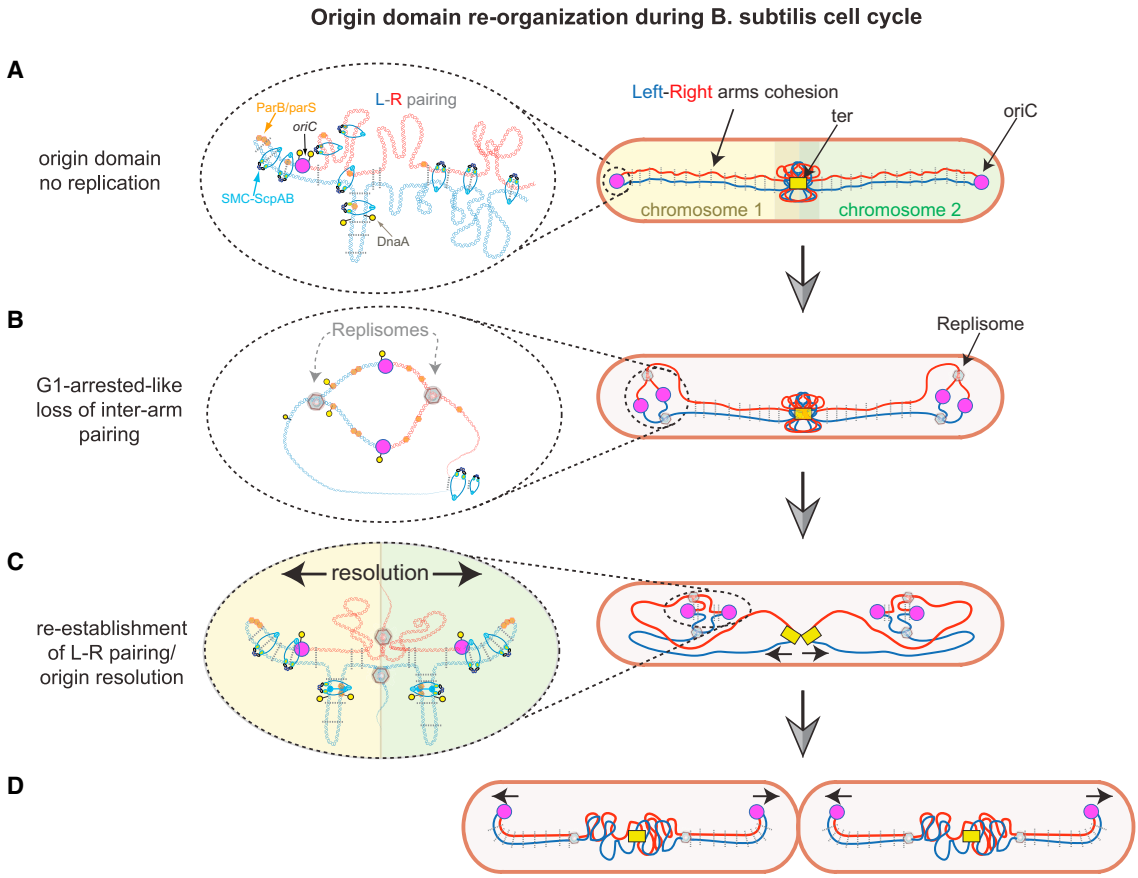

Figure 7. Model of Origin Domain and Chromosome Organization during *B. subtilis* Cell Cycle

(A) In nascent cells, the right and left replichores (in blue and red) are zipped (gray dotted lines) by the action of ParB/*parS* (orange hexagons) and SMC-ScpAB (indicated in the figure) complexes. SMC-ScpAB proteins also are responsible for intra-arm pairing. Pink and yellow circles: oriC and DnaA boxes, respectively. The ter region is not yet resolved.

(B) During early replication, inter-arm contacts are disrupted to establish a G1-arrest-like configuration. This disruption can later propagate to the remainder of the chromosome. Grey/bright hexagons: replisomes.

(C) Re-organization of the origin region occurs concomitantly with origin migration to the middle of new nucleoids. Newly replicated origins are resolved by the action of the ParABS partition system and SMC-ScpAB. Left-right replichore pairing is re-established at the origin domain. The recently replicated ter region starts to be resolved into the daughter cells.

(D) Origins are completely segregated to the nucleoid poles, and the structures formed at nascent origin domains are propagated to the remainder of the chromosome, possibly coupling chromosome segregation and cell division.

occurring specifically at the middle of new nucleoids (Figure 6). This origin re-localization may be accompanied by a general reorganization of the origin domain in which inter-arm replichore contacts are disrupted to establish a G1-arrest-like configuration (Figure 7B). The signals and processes coupling changes in origin domain structure to origin firing remain to be elucidated. The most straightforward possibility is that initiation of DNA replication may trigger the unfolding of the origin domain coupled to dissociation of ParB/SMC-ScpAB. Alternatively, unidentified factors/processes may initiate origin firing, triggering the ensuing structural re-organization and re-localization of the origin region.

After reaching their new mid-nucleoid positions, origin domains may promptly re-establish their original folding by pairing replichores together through SMC-ScpAB-mediated intra- and inter-arm contacts (Figure 7C). The establishment of this condensed origin structure requires the ParBS partition system, the SMC-ScpAB complex, and active replication (Figures 3 and 5), supporting the role of condensin complexes in the resolution of newly replicated origins (Gruber et al., 2014; Wang et al., 2014b). Replichore re-zipping is presumably initiated from the cluster of *parS* sites ($parS^{354,355,356}$) (Figures 2 and 3), consistent with similar observations in *C. crescentus* (Umbarger et al., 2011). The re-folding of the origin domain after replication could thus serve to inhibit replication initiation until the next cell cycle. Consistently, deletion of parB and DnaA boxes leads to severe chromosome segregation defects that can be suppressed by mutations in a replicator inhibitor (ParA) (Okumura et al., 2012). In addition, fast and ordered re-folding of newly replicated origins may optimize their resolution by limiting DNA catenation between sister chromatids (Gruber et al., 2014). Finally, origin re-folding would allow the ParABS partition machinery to recognize pairs of replicated origins for segregation into different

directions, mirroring the role of eukaryotic centromeres in allowing the spindle to recognize pairs of replicated products during mitosis.

Roles of SMC-ScpAB in Chromosome Pairing

Inter-arm pairing is first established at the newly replicated origins but gradually extends to the remainder of the chromosome with the progression of replication (Figure 3). SMC-ScpAB complexes are recruited to the origin region by specific contacts with ParB (Gruber and Errington, 2009; Sullivan et al., 2009) but may subsequently shift from *parS* sites to promote long-range contacts along the entire replichores (Figures 1B and 2C). Overall, these observations are consistent with a model in which SMC-ScpAB complexes (1) are recruited to the origin region, where they convert to a topologically closed ring encompassing two or more double-stranded DNA segments (Wilhelm et al., 2015); (2) diffuse/slide away from the recruitment site in a closed-ring conformation, maintaining cohesion between replichores; and (3) break open in a stochastic or regulated fashion, probably requiring nucleotide hydrolysis. This model is consistent with two populations of SMC-ScpAB coexisting in the cell: a static population at the origin, and a highly mobile population that appears to scan the nucleoid (Kleine Borgmann et al., 2013). The concomitant spreading of replichore pairing with replication may occur in a regular or discontinuous manner and may help in condensation of the two newly replicated chromosomes to facilitate segregation (Gruber et al., 2014; Wang et al., 2014b). The re-establishment of a precise and ordered longitudinal choreography may be essential to promptly act upon external stimuli to induce developmental changes (e.g., *oriC*-tethering to cell pole early in sporulation) and to re-initiate normal chromosome choreography during spore germination.

Despite the apparent simplicity of bacterial chromosomes and their lack of constitutive chromatin, several fundamental principles of eukaryotic higher-order DNA organization are present in this kingdom. It is tempting to hypothesize that the mechanism of recruitment and spread of SMC-ScpAB, as well as the role of ParABS, may be paralleled to the mechanisms employed by condensins/cohesins and chromatin insulators in eukaryotes. Excitingly, our results represent a striking example of how the 3D folding dynamics of the chromosome fiber itself may be functionally coupled to other DNA management processes and involved in its own regulation.

EXPERIMENTAL PROCEDURES

General Methods

B. subtilis strains were derived from either the prototrophic strains PY79 or BS168. The strains used are listed in Table S1. The construction of plasmids is described in the Supplemental Experimental Procedures and Table S2. Cells were grown in minimal and rich media at 30°C. Cell synchronizations were performed as previously described with minor changes. Refer to Supplemental Experimental Procedures for more details.

3D-SIM and 3D-PALM

3D-SIM imaging was performed on an OMX V3 microscope (Applied Precision) as previously described (Fiche et al., 2013). Reconstruction and alignment of 3D-SIM images was performed using softWoRx v5.0 (Applied Precision). 3D-PALM imaging was performed as described previously (Cattoni et al., 2013; Fiche et al., 2013). For 3D-PALM, a MicAO 3D-SR module (Imagine Optic) was used. Refer to Supplemental Experimental Procedures for more details.

Hi-C

Chromosome conformation capture experiments were performed as described elsewhere (Marbouty et al., 2014). Sequencing data were processed into genome-wide contact maps (4 kb bins) that were normalized using the sequential component normalization procedure described previously (Marbouty et al., 2014). The accession number for the sequences reported in this paper is BioProject: PRJNA289589. http://www.ncbi.nlm.nih.gov/bioproject/289589. Raw, 4 kb resolution contact maps are available in Data S1. Full details are provided in Tables S3 and S4 and Supplemental Experimental Procedures.

ACCESSION NUMBERS

The accession number for the sequences reported in this paper is BioProject: PRJNA289589.

SUPPLEMENTAL INFORMATION

Supplemental Information includes Supplemental Experimental Procedures, six figures, four tables, two movies, and one data file and can be found with this article online at http://dx.doi.org/10.1016/j.molcel.2015.07.020.

AUTHOR CONTRIBUTIONS

Investigation, A.L.G., D.I.C., M.M., and J-B.F.; Data curation, A.L.G, M.N., and A.C.; Formal analysis, A.L.G., M.N., R.K., A.C., J-B.F., M.M., and J.M.; Software, A.L.G, M.N., J-B.F., and J.M.; Methodology, A.L.G., D.I.C., M.N., J-B.F., and R.K.; Conceptualization, M.N., R.K., A.L.G, and D.I.C; Writing – original draft, M.N., R.K., A.L.G., and D.I.C.; Writing – review and editing, M.N. and R.K.; Funding acquisition, M.N., H.M., and R.K.; Resources, A.K., H.M., and J.M.; Supervision, M.N. and R.K.

ACKNOWLEDGMENTS

We thank J. Bonnet and O. Espeli for critical reading of the manuscript, Marie Schaeffer for her ideas on data interpretation, A. Rappailles for help in preparation of initial 3C/Hi-C libraries, and A. Grossman for strains. We also thank D. Rudner and co-workers for sharing strains and for communicating openly. Research was supported by European Research Council Starting Grants to R.K. (ERC-Stg-260822) and M.N. (ERC-Stg-260787) and by a Royal Society University Research Fellowship and a BBSRC Research Grant (BB/K017527/1) to H.M. M.M. is the recipient of a fellowship from the Association pour la Recherche sur le Cancer (20100600373). 3D-SIM experiments were performed at Montpellier RIO imaging. We acknowledge support from France-BioImaging (FBI, ANR-10-INSB-04) and Imagine Optic.

Received: November 23, 2014
Revised: June 10, 2015
Accepted: July 21, 2015
Published: August 20, 2015

REFERENCES

Berkmen, M.B., and Grossman, A.D. (2006). Spatial and temporal organization of the *Bacillus subtilis* replication cycle. Mol. Microbiol. *62*, 57–71.

Berkmen, M.B., and Grossman, A.D. (2007). Subcellular positioning of the origin region of the Bacillus subtilis chromosome is independent of sequences within oriC, the site of replication initiation, and the replication initiator DnaA. Mol. Microbiol. *63*, 150–165.

Booker, B.M., Deng, S., and Higgins, N.P. (2010). DNA topology of highly transcribed operons in Salmonella enterica serovar Typhimurium. Mol. Microbiol. *78*, 1348–1364.

Breier, A.M., and Grossman, A.D. (2007). Whole-genome analysis of the chromosome partitioning and sporulation protein Spo0J (ParB) reveals spreading and origin-distal sites on the Bacillus subtilis chromosome. Mol. Microbiol. *64*, 703–718.

Cattoni, D.I., Fiche, J.-B., Valeri, A., Mignot, T., and Nöllmann, M. (2013). Super-resolution imaging of bacteria in a microfluidics device. PLoS ONE *8*, e76268.

Dekker, J., Rippe, K., Dekker, M., and Kleckner, N. (2002). Capturing chromosome conformation. Science *295*, 1306–1311.

Dixon, J.R., Selvaraj, S., Yue, F., Kim, A., Li, Y., Shen, Y., Hu, M., Liu, J.S., and Ren, B. (2012). Topological domains in mammalian genomes identified by analysis of chromatin interactions. Nature *485*, 376–380.

Fiche, J.B., Cattoni, D.I., Diekmann, N., Langerak, J.M., Clerte, C., Royer, C.A., Margeat, E., Doan, T., and Nöllmann, M. (2013). Recruitment, assembly, and molecular architecture of the SpoIIIE DNA pump revealed by superresolution microscopy. PLoS Biol. *11*, e1001557.

Fisher, J.K., Bourniquel, A., Witz, G., Weiner, B., Prentiss, M., and Kleckner, N. (2013). Four-dimensional imaging of *E. coli* nucleoid organization and dynamics in living cells. Cell *153*, 882–895.

Gruber, S., and Errington, J. (2009). Recruitment of condensin to replication origin regions by ParB/SpoOJ promotes chromosome segregation in *B. subtilis*. Cell *137*, 685–696.

Gruber, S., Veening, J.-W., Bach, J., Blettinger, M., Bramkamp, M., and Errington, J. (2014). Interlinked sister chromosomes arise in the absence of condensin during fast replication in *B. subtilis*. Curr. Biol. *24*, 293–298.

Hadizadeh Yazdi, N., Guet, C.C., Johnson, R.C., and Marko, J.F. (2012). Variation of the folding and dynamics of the Escherichia coli chromosome with growth conditions. Mol. Microbiol. *86*, 1318–1333.

Higgins, N.P. (2014). RNA polymerase: chromosome domain boundary maker and regulator of supercoil density. Curr. Opin. Microbiol. *22*, 138–143.

Ishikawa, S., Ogura, Y., Yoshimura, M., Okumura, H., Cho, E., Kawai, Y., Kurokawa, K., Oshima, T., and Ogasawara, N. (2007). Distribution of stable DnaA-binding sites on the Bacillus subtilis genome detected using a modified ChIP-chip method. DNA Res. *14*, 155–168.

Kleckner, N., Fisher, J.K., Stouf, M., White, M.A., Bates, D., and Witz, G. (2014). The bacterial nucleoid: nature, dynamics and sister segregation. Curr. Opin. Microbiol. *22*, 127–137.

Kleine Borgmann, L.A.K., Ries, J., Ewers, H., Ulbrich, M.H., and Graumann, P.L. (2013). The bacterial SMC complex displays two distinct modes of interaction with the chromosome. Cell Rep. *3*, 1483–1492.

Le, T.B.K., Imakaev, M.V., Mirny, L.A., and Laub, M.T. (2013). High-resolution mapping of the spatial organization of a bacterial chromosome. Science *342*, 731–734.

Lesne, A., Riposo, J., Roger, P., Cournac, A., and Mozziconacci, J. (2014). 3D genome reconstruction from chromosomal contacts. Nat. Methods *11*, 1141–1143.

Marbouty, M., Cournac, A., Flot, J.-F., Marie-Nelly, H., Mozziconacci, J., and Koszul, R. (2014). Metagenomic chromosome conformation capture (meta3C) unveils the diversity of chromosome organization in microorganisms. eLife *3*, e03318.

Nasmyth, K., and Haering, C.H. (2009). Cohesin: its roles and mechanisms. Annu. Rev. Genet. *43*, 525–558.

Nicolas, P., Mäder, U., Dervyn, E., Rochat, T., Leduc, A., Pigeonneau, N., Bidnenko, E., Marchadier, E., Hoebeke, M., Aymerich, S., et al. (2012). Condition-dependent transcriptome reveals high-level regulatory architecture in Bacillus subtilis. Science *335*, 1103–1106.

Okumura, H., Yoshimura, M., Ueki, M., Oshima, T., Ogasawara, N., and Ishikawa, S. (2012). Regulation of chromosomal replication initiation by oriC-proximal DnaA-box clusters in Bacillus subtilis. Nucleic Acids Res. *40*, 220–234.

Postow, L., Hardy, C.D., Arsuaga, J., and Cozzarelli, N.R. (2004). Topological domain structure of the Escherichia coli chromosome. Genes Dev. *18*, 1766–1779.

Sexton, T., Yaffe, E., Kenigsberg, E., Bantignies, F., Leblanc, B., Hoichman, M., Parrinello, H., Tanay, A., and Cavalli, G. (2012). Three-dimensional folding and functional organization principles of the Drosophila genome. Cell *148*, 458–472.

Smits, W.K., and Grossman, A.D. (2010). The transcriptional regulator Rok binds A+T-rich DNA and is involved in repression of a mobile genetic element in Bacillus subtilis. PLoS Genet. *6*, e1001207.

Smits, W.K., Merrikh, H., Bonilla, C.Y., and Grossman, A.D. (2011). Primosomal proteins DnaD and DnaB are recruited to chromosomal regions bound by DnaA in Bacillus subtilis. J. Bacteriol. *193*, 640–648.

Sullivan, N.L., Marquis, K.A., and Rudner, D.Z. (2009). Recruitment of SMC by ParB-*parS* organizes the origin region and promotes efficient chromosome segregation. Cell *137*, 697–707.

Umbarger, M.A., Toro, E., Wright, M.A., Porreca, G.J., Baù, D., Hong, S.-H., Fero, M.J., Zhu, L.J., Marti-Renom, M.A., McAdams, H.H., et al. (2011). The three-dimensional architecture of a bacterial genome and its alteration by genetic perturbation. Mol. Cell *44*, 252–264.

Wang, X., Montero Llopis, P., and Rudner, D.Z. (2014a). Bacillus subtilis chromosome organization oscillates between two distinct patterns. Proc. Natl. Acad. Sci. USA *111*, 12877–12882.

Wang, X., Tang, O.W., Riley, E.P., and Rudner, D.Z. (2014b). The SMC condensin complex is required for origin segregation in Bacillus subtilis. Curr. Biol. *24*, 287–292.

Wilhelm, L., Bürmann, F., Minnen, A., Shin, H.-C., Toseland, C.P., Oh, B.-H., and Gruber, S. (2015). SMC condensin entraps chromosomal DNA by an ATP hydrolysis dependent loading mechanism in *Bacillus subtilis*. Elife *4*, http://dx.doi.org/10.7554/eLife.06659.